Novel gas sensor with dual response under CO(g) exposure: Optical and electrical stimuli

L.S.R. Rocha [a],[*], M. Cilense [b], M.A. Ponce [c], C.M. Aldao [c], L.L. Oliveira [a], E. Longo [b], A.Z. Simoes [a]

[a] Sao Paulo State University (UNESP), School of Engineering, Av. Dr Ariberto Pereira da Cunha 333, Bairro Pedregulho, CEP 12.516-410, Guaratinguetá, São Paulo, Brazil
[b] Sao Paulo State University (UNESP), Institute of Chemistry, CEP 14801-907, Araraquara, São Paulo, Brazil
[c] Institute of Materials Science and Technology Investigation (INTEMA), Juan B. Justo 4302, 7600, Mar del Plata, Argentina

ABSTRACT

In this work, a lanthanum (La) doped ceria (CeO_2) film, which depicted a dual gas sensing response (electric and optical) for $CO_{(g)}$ detection, was obtained by the microwave-assisted hydrothermal (HAM) synthesis and deposited by the screen-printing technique, in order to prevent deaths by intoxication with this life-threatening gas. An electric response under $CO_{(g)}$ exposure was obtained, along with an extremely fast optical response for a temperature of 380 °C, associated with Ce^{+4} reduction and vacancy generation. A direct optical gap was found to be around 2.31 eV from UV–Vis results, which corresponds to a transition from valence band to 4f states. Due to the anomalous electron configuration of cerium atoms with 4f electrons in its reduced state, they are likely to present an electric conduction based on the small polaron theory with a hopping mechanism responsible for its dual sensing response with a complete reversible behaviour.

© 2017 Elsevier B.V. All rights reserved.

1. Introduction

Ceria (CeO_2) has been considered an important nanomaterial for applications in catalysis [1,2], fuel cells [3], ultraviolet absorbers [4], hydrogen storage materials [5], oxygen sensors [6], optical devices [7], polishing materials [8], and for which the use of nanocrystalline powders is an important factor [9]. Several methods have been developed to prepare ultra-fine CeO_2 powder, including hydrothermal [10], precipitation (for oxalate [11], carbonate [12,13], peroxide [9], hydroxide [14], polymeric precursor [15,16], complexion with citric acid [15], the flow method [17], organometallic decomposition [18] and microwave-assisted heating technique [19–21]. Among the various methods, the hydrothermal crystallization is an interesting process to directly prepare pure fine oxide powders with reduced contamination and low synthesis temperature. The conventional hydrothermal method requires longer soaking times at a low temperature (below 200 °C) to obtain the ceria powders. For this reason, the introduction of microwave heating to the conventional hydrothermal method is advantageous for the synthesis of various ceramic powders because the microwave heating permits a reduction of processing time and energy cost. Particles with desired size and shape can be produced if parameters such as solution pH, reaction temperature, reaction time, solute concentration and the type of solvent are carefully monitored [22]. A modification of the hydrothermal method developed by Komarneni et al. [23–25] involves the introduction of microwaves during the hydrothermal synthesis to increase the kinetics of crystallization by one to two orders of magnitude compared to the conventional hydrothermal. The microwave-assisted hydrothermal (MAH) method shows advantages such as rapidity, convenience, and cost-effectiveness. Ceria systems with nanosized particles were successfully synthesized by the MAH method utilizing a relatively low temperature and short reaction time [26]. In this present work, the authors describe the conditions of formation of the ceria via MAH, introduce the advantages of microwave irradiation method and also report in details the method used. In previous work, our group worked on the preparation of CeO_2 films coming from nanostructures obtained by the microwave-hydrothermal methods and its gas sensing measurements have been carried out to rationalize the type and number of surface adsorbed groups and overall nanostructure. Variations of electrical conductance, as a consequence of gases adsorption onto semiconductor oxide film surfaces, were observed [27]. In polycrystalline materials, it is widely accepted that barriers formed between particles or grains have a Schottky-type nature and that they govern the electrical behaviour. Adsorption of gaseous species at the grain boundaries can induce changes in the barrier heights and in the donor

---

* Corresponding author.
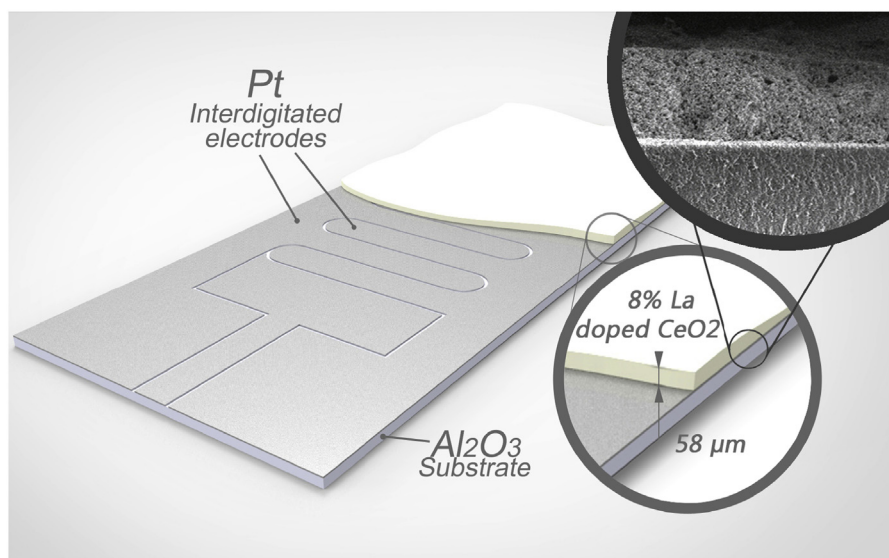 *E-mail address:* drleandrosrr@gmail.com (L.S.R. Rocha).

Fig. 1. Substrate with the interdigitated electrodes deposited by a home-built micromachining laser along with the 8% La-doped film deposited.

concentrations. Most researchers in the field consider that many oxide semiconductors have a large number of oxygen vacancies, conferring their *n*-character, with cerium oxide being a potential candidate [28,29]. It is known that oxygen is chemisorbed on the surface of the oxide, increasing the barrier height and width of surface barriers. In this fast process, the equilibrium with atmospheric oxygen would be reached rapidly. Subsequently, in a second process, we found for metal oxide semiconductors that oxygen diffuses slowly into the grains (at temperatures above 200 °C), annihilating vacancies and reducing the donor concentration. Besides, as was proposed by Tuller et al. and Wuilloud et al. [30,31], rare-earth oxides with 4f-shells of the lanthanide ions are likely to present narrow bands and then the electrical conduction would involve 4f electrons that migrate by an activated hopping mechanism.

The pure CeO_2 is a poor ionic conductor with a band gap of 6 eV [31] adopting the fluorite structure (space group Fm3m) with singly or doubly ionized oxygen vacancies ($V_O·,V_Ö$) as the predominant ionic defect. Ceria-based electrolytes have been extensively studied and made much progress. In particular, some singly doped-electrolytes can be obtained by doping the ceria host structure with other cations, such as $Ce_{1-x}Gd_xO_{2-\delta}$, $Ce_{1-x}Sm_xO_{2-\delta}$, $Ce_{1-x}Y_xO_{2-\delta}$, showing high oxide ion conductivity at intermediate temperatures (500–700 °C) [32–36]. Various rare-earth doped ceria systems (La, Sm, Pr) have successfully been prepared by hydrothermal treatment, providing low-temperature preparation and morphological control of ultrafine particles of uniform crystallite dimension [37–39]. Replacement of Ce^{4+} with divalent or trivalent ions results in the creation of oxygen vacancies [40], and the choice of the dopant is usually advocated by the ability of the dopant to minimize the internal strain of the lattice [41–43]. Therefore, we show, in the present study the role of lanthanum (La) doping on the structure and chemistry of ceria thin films and the resultant variation in the resistance under $CO_{(g)}$ atmosphere. The main goal of lanthanum addition, with a lower valence state of La^{3+} (r = 0.110 nm) than Ce^{4+} (r = 0.097 nm), was to reduce the conductivity, along with a lattice expansion, resulting in an improvement of the CO sensing properties.

2. Experimental procedure

Lanthanum doped CeO_2 nanopowder was synthesized by the microwave-assisted hydrothermal method. The experimental procedure was based on the dissolution of cerium (III) nitrate hexahydrate [Ce(NO)$_3$·6H$_2$O; 99%-Sigma] in an aqueous medium, under constant magnetic stirring. Separately, lanthanum oxide (La$_2$O$_3$) (99% purity - Aldrich) was dissolved in a nitric acid medium and added to the solution. The resulting mixture was heated at 70 °C under stirring and its pH adjusted through the addition of basic aqueous solution 2 mol L^{-1} of KOH (99.5% purity - Synth) until a pH~10. The resulted solution was transferred into a sealed Teflon autoclave and placed in a hydrothermal microwave (2.45 GHz, 800 W). The reaction system was heat-treated at 100 °C for 8 min with a heating rate fixed at 10 °C/min and then allowed to cool naturally. The nanopowders were centrifuged and washed with deionized water and then dried in a laboratory oven at 100 °C for 2 days. The obtained nanostructures were characterized by X-ray powder diffraction (XRD) using a (Rigaku-DMax/2500PC, Japan) with Cu-Kα radiation (λ = 1.5406 E) in the 2θ range from 20 to 80° with 0.2 °/min. The crystallite size d was calculated using Scherrer equation $d = \frac{0.94\lambda}{\beta \cdot \cos\theta}$, where λ is the wavelength of X-rays, β is the full width at half maximum (FWHM) for (1 1 1) reflection, and θ is the diffraction angle of the main peak. The obtained powder was used to prepare a film through the screen-printing technique based on a paste composed of an organic binder (glycerol) using a solid/organic binder ratio of 0.6 g/mL. The used substrates were composed of 96% dense insulating alumina (Al$_2$O$_3$), on which electrodes with an interdigitated shape had been delineated by sputtering. An adhesion layer consisting of 25 nm titanium (Ti) was deposited and, without breaking the vacuum, a platinum (Pt) 200 nm film was deposited over the Ti layer. For defining the interdigitated electrodes, the substrates with the metal films were placed in a home-built micromachining laser, producing the substrate seen in Fig. 1. Later, films were thermally treated in dry air atmosphere up to 380 °C and maintained at this temperature for 2 h, using a heating rate of 1 °C/min in order to evaporate the binder. The FT-IR spectra were recorded with a Rayleigh – WQF-510A model spectrometer in transmittance mode. Infrared spectroscopy was used for monitoring some of the structural modifications occurring during the synthesis process with the KBr pellet technique. Ultraviolet–visible (UV–vis) spectroscopy for the optical absorbance spectra was taken using a Cary 5G (Varian, USA) spectrophotometer in diffuse reflection mode. The morphology of film surface was observed using a high-resolution field-emission gun scanning electron microscope (FEG-SEM) Supra 35-VP (Carl Zeiss, Germany). The electrical resistance
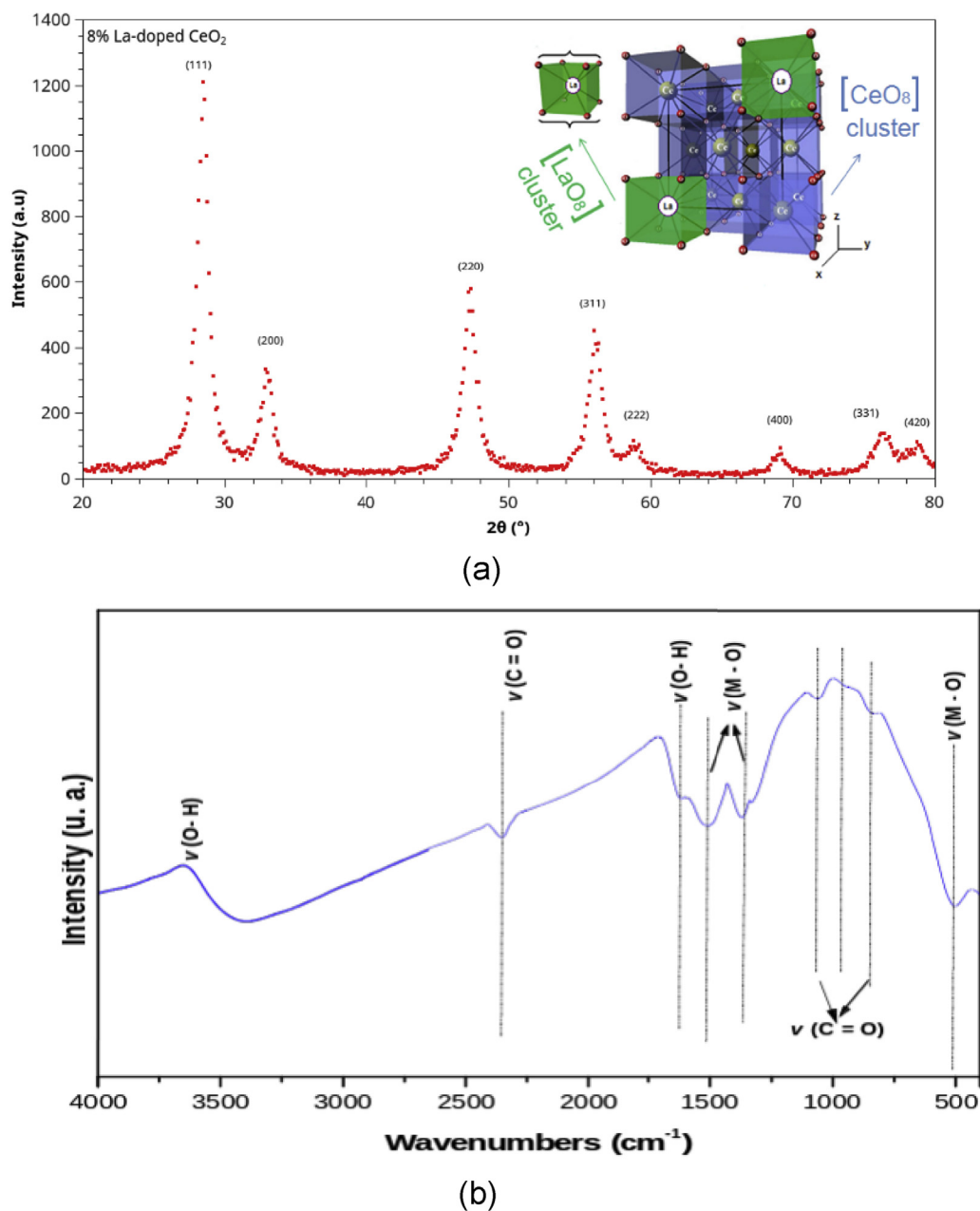
Fig. 2. (a) XRD pattern of the La-doped CeO$_2$ nanostructures synthesized at 100 °C in the MAH method under KOH mineralizer. Inset shows the lanthanum substituted CeO$_8$ clusters and (b) FT-IR spectroscopy of the La-doped CeO$_2$ nanostructures synthesized at 100 °C in the MAH method under KOH mineralizer.

characterization of films were measured during a temperature variation as well as with time variation in a temperature of 400 °C, to be close to that observed for the optical response (~380 °C) and to the working temperature, achieved at a rate of ~2 °C/min in vacuum, dry air and in CO atmosphere, with a constant pressure of 50 mmHg, during the entire cycling. Worth to mention that the electrical measurements were done in a device for the optoelectronic characterization of materials (Patent INPI Argentina 201501039539/INPI Brazil 10 2016 028383 3 [44,45]) which consists of a closed chamber and that three cycles of heating in vacuum, up to 380 °C were made before measuring the resistance values, assuring the volatilization of any humidity. Measurements were done when samples get to steady state and no changes in resistance over time were observed, with an applied magnitude of excitation current of 1 mA, obtained using the two-wire technique with a DC-type measurement. As we previously mention, the alumina substrates were electrically measured and showed an

insulating behaviour with no influence on the film total electrical response. An Agilent 3440A multimeter was used for the electrical resistance measurements. For the specific surface area measurements, samples were treated in a conventional oven at 350 °C for 24 h in order to remove all humidity followed by calculations on a Micromeritics ASAP 2010 using the BET method.

3. Results and discussion

Fig. 2a illustrates the XRD of La-doped ceria nanostructures obtained by the MAH route at 100° C for 8 min prepared with KOH (2 M). To provide the formation of solid solution we have carried out the partial replacement of Ce ions with trivalent lanthanum ion in an 8% mol concentration. It is known that rare earth doped ceria could create a corresponding number of anion vacancies and result in a solid solution with high ionic conductivity, producing a

defective surface which may enhance their sensing properties, and also that lanthanum can avoid the ceria crystallite to grow in severe oxidizing environments, acting as stabilizer [46]. Analyzing the pattern of the crystalline sample, it is found that upon insertion of La, all of the peaks could be well-indexed to a pure cubic structure of CeO_2 (space group: Fm3m) with lattice constant a = 5.411 Å, which is in good agreement with the JCPDS file for CeO_2 (JCPDS 34-394). The average crystallite size calculated by Scherrer method was 4.20 nm. The insertion of lanthanum leads to a redistribution of charge density, which can be associated with its greater radial stabilizing effect of oxygen vacancies [27]. The inset depicts the $[CeO_8]$ clusters being modified by the insertion of lanthanum, which substitutes the cerium ions generating lattice distortions. A clear evidence that CeO_2 is formed instead $Ce(OH)_x$ come from the fact that nitrate salts of ceria were preferably used since these salts were easily dissociable in few milliliters of water and the formed species (Ce^{4+}), after treating with acid, reacted spontaneously with the mineralizer to produce a highly exothermic reaction. When cerium nitrate is used as the precursor salt and reacted with an acid to dissolve it, the Ce^{3+} ion is oxidized to Ce^{4+} ion and them acidic mass reacts exothermically with the mineralizer, forming a by-product salt (KNO_3) that surrounds the hydroxide product avoiding its overrated growth. In the oxidizing atmosphere, dehydration occurs, converting the hydroxide intermediate to oxide. In the MAH methods, the conversion to oxide is more rapid due to the effect of energetic radiations assisting the transformation to CeO_2 instead $Ce(OH)_x$.

The FT-IR spectra in the range 4000–400 cm^{-1} of as-synthesized samples are shown in Fig. 2b. The bands at 3400 cm^{-1} and 1600 cm^{-1} can be attributed to the O–H vibration in absorbed water molecules on the sample surface [47–50]. The band at 2300 cm^{-1} can be attributed to the C=O vibration in CO_2 present in the air, as well as those observed in the region around 1000 cm^{-1}. The FT-IR bands at about 1500, 1350, 1000 and 900 cm^{-1}, are similar to those of commercial CeO_2 powders [51] and CeO_2 nanoparticles [52]. The strong broadband below 700 cm^{-1} which is due to the envelope of the phonon band of the metal oxide network [51]. In hydrothermal-microwave processing, the high-frequency electromagnetic radiation interacts with the permanent dipole of the liquid (H_2O) which initiates rapid heating from the resultant molecular rotation. Also, permanent or induced dipoles in the dispersed phase cause rapid heating of the particles which results in a reaction temperature in excess of the surrounding liquid-localized superheating. Following the literature, hydrolysis refers to those reactions of metallic ions with water that liberate protons and produce hydroxide or oxide solids. Ce^{4+} ions, which have a low basicity and high charge, undergo strong hydration. Firstly, Ce^{4+} ions are hydrolyzed and form complexes with water molecules or OH^- to give $[Ce(OH)_x(H_2O)_y]^{(4-x)+}$, where x + y is the coordination number of Ce^{4+}. Further polymerization is likely, and both species can serve as the precursors for the final ceria nanoparticles. In an aqueous solution, H_2O, being a polar molecule, tends to take protons away from coordinated hydroxide, leading to the formation of $CeO_2 \cdot nH_2O$. This process can be described by the following equations [41]:

$$Ce^{4+} + xOH + yH_2O \rightarrow [Ce(OH)_x(H_2O)_y]^{(4-x)+} \tag{1}$$

$$[Ce(OH)_x(H_2O)_y]^{(4-x)+} + H_2O \rightarrow CeO_2.nH_2O + nH_2O + H_3O^+ \tag{2}$$
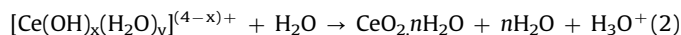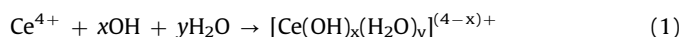
Fig. 3 illustrates the UV–Vis spectrum of the La-doped CeO_2 nanostructures synthesized at 100 °C for 8 min in the MAH method under KOH mineralizer. The optical band gap energy (E_{gap}) was calculated by the method proposed by Kubelka and Munk [40]. This methodology is based on the transformation of diffuse reflectance measurements to estimate E_{gap} values with good accuracy within the limits of assumptions when modelled in three dimensions [46]. Particularly, it is useful in limited cases of an infinitely thick sample layer. The Kubelka-Munk equation for any wavelength is described by Eq. (3):

$$F(R_\infty) = (1 - R_\infty)^2/2R_\infty = k/s \tag{3}$$

where $F(R_\infty)$ is the Kubelka-Munk function or absolute reflectance of the sample. In our case, magnesium oxide (MgO) was the
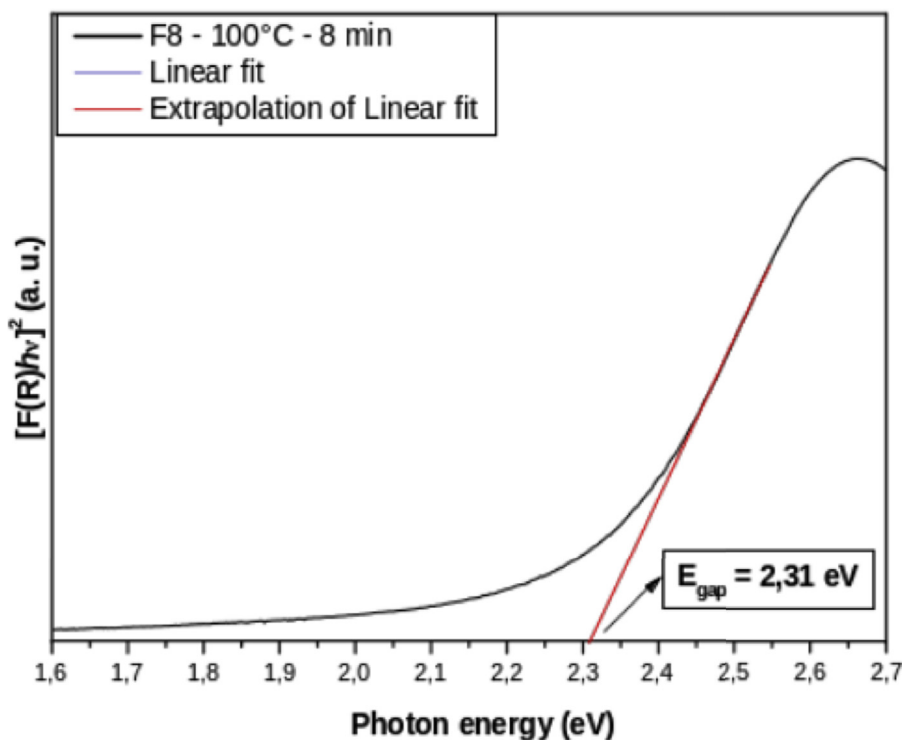

Fig. 3. UV–Vis spectra of La-doped CeO_2 nanostructures synthesized at 100 °C for 8 min in the MAH method.

standard sample in reflectance measurements. $R_\infty = R_{sample}/R_{MgO}$ (R_∞ is the reflectance when the sample is infinitely thick), k is the molar absorption coefficient and s is the scattering coefficient. In a parabolic band structure, the optical band gap and absorption coefficient of semiconductor oxides [47] can be calculated by Eq. (4):

$$\alpha h\nu = C_1(h\nu - E_{gap})^n \qquad (4)$$

where α is the linear absorption coefficient of the material, $h\nu$ is the photon energy, C_1 is a proportionality constant, E_{gap} is the optical band gap and n is a constant associated with different kinds of electronic transitions (n = 0,5 for a direct allowed, n = 2 for an indirect allowed, n = 1,5 for a direct forbidden and n = 3 for an indirect forbidden). According to the literature [48], the CeO_2 nanoparticles exhibit an optical absorption spectrum governed by direct electronic transitions. In this phenomenon, after the electronic absorption process, the electrons located in the maximum-energy states in the valence band revert to minimum-energy states in the conduction band at the same point in the Brillouin zone [49]. Based on this information, E_{gap} values were calculated using n = 0.5 in Eq. (4). Finally, using the remission function described in Eq. (3) and with the term k = 2α, we obtain the modified Kubelka–Munk equation indicated in Eq. (5):

$$[F(R_\infty)h\nu]^2 = C_2(h\nu - E_{gap}) \qquad (5)$$

Therefore, finding the $F(R_\infty)$ value from Eq. (5), and plotting a graph of $[F(R_\infty)h\nu]^2$ against $h\nu$, the extrapolation of the linear portions of the curves towards absorption equal to zero (y = 0) gives E_{gap} for direct transitions. The estimated direct E_{gap} of the sample is shown in the figure. The uncertainty of these values was estimated at 0.05 eV. The band gap of CeO_2 reported in this work is lower than that reported in the literature. Phokha et al. [50] reported direct band gap values ranging from 3.00 to 3.10 eV for monodisperse CeO_2 nanospheres synthesized by PVP-assisted hydrothermal method and Palard et al. [51] reported estimated band gaps ranging between 3.56 and 3.76 eV for undoped and doped cerium oxide nanoparticles with the following chemical formula: $Ce_{1-x}M_xO_{2-(x/2)}$ (M = Y or Gd and x = 0 or 0.15) by different co-precipitation protocols at room temperature.

Fig. 4 (a) shows the SEM image of the film, obtained from the La-doped nanopowder synthesized under MAH conditions on KOH (2 M) mineralizer agent with a soaking time of 8 min, which depicted a specific surface area of 86 m^2/g against 120 m^2/g for the pure sample. Due to the extremely reduced particles size, within the nanometer range, along with the usage of a ligand solution to deposit the film, these tend to form a high degree of agglomeration caused by Van der Waal's force derived for the hydroxyl groups (−OH) from the glycerol. Micrometric and anisotropic agglomerates obtained in this study are quite similar to the lanthanum-doped ceria samples obtained by K. Singh et al. [52] with a co-precipitation method, calcined at 1350 °C for 2 h, depicting formations with more than 2 μm length and a distinct trapezoid-type morphology. Worth to mention that the average thicknesses of the pure sample, manually deposited by a screen-printing technique was close to 58 μm whilst the 8% La doped sample presented an average thickness of 56 μm, as seen in Fig. 4 (b) and (c). Particle analysis by means of the ImageJ software was performed on Fig. 4 (a), showing an average porosity of up to 33.59% and an average pore size of 0.613 μm.

In Fig. 5 (a) and (b), relative responses under 50 mmHg of oxygen or CO were measured for different temperatures as R_{gas}/R_v, where R_{gas} corresponds to the resistance of films when they reach equilibrium after oxygen R_{O2} or CO R_{CO} exposition respectively, at different temperatures, and R_v is the resistance of films in vacuum. As temperature rises, the films presented an increasing response when exposed to air. This can be associated with oxygen adsorption at the particle surfaces producing a decrease in the sample
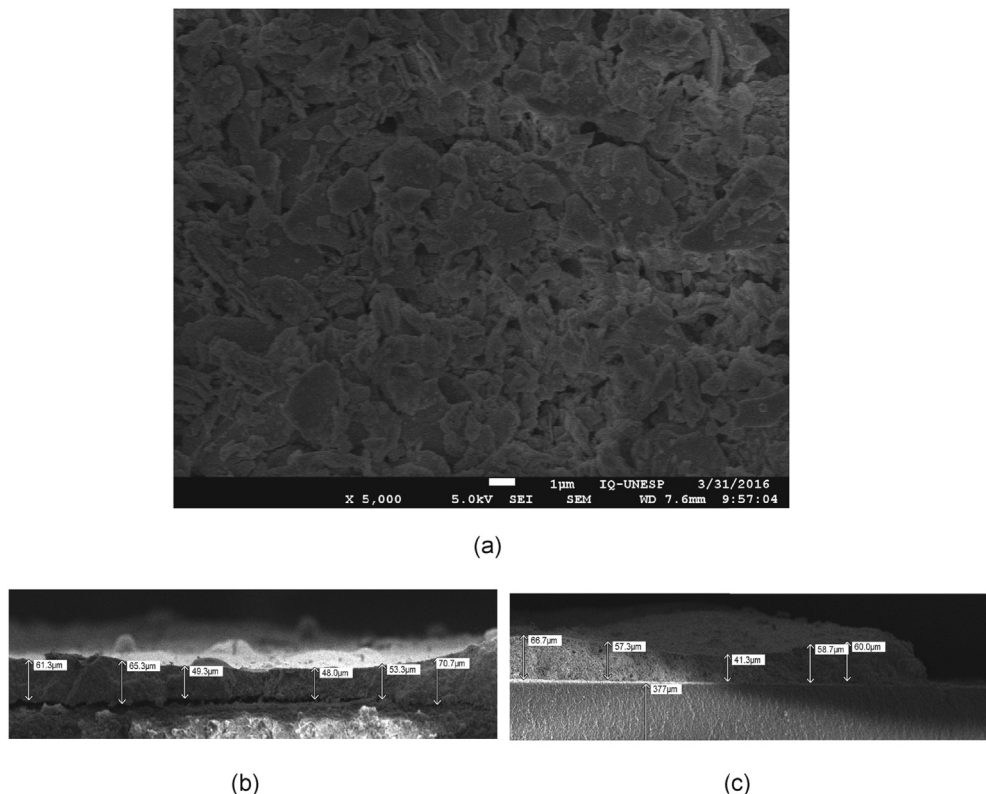

(a)

(b)

(c)

Fig. 4. (a) FEG-SEM of the La-doped film obtained from the nanostructures synthesized at 100 °C for 8 min in the MAH method under KOH mineralizer along with a cross-sectional view for the pure (b) and doped (c) films.

(a)

(b)

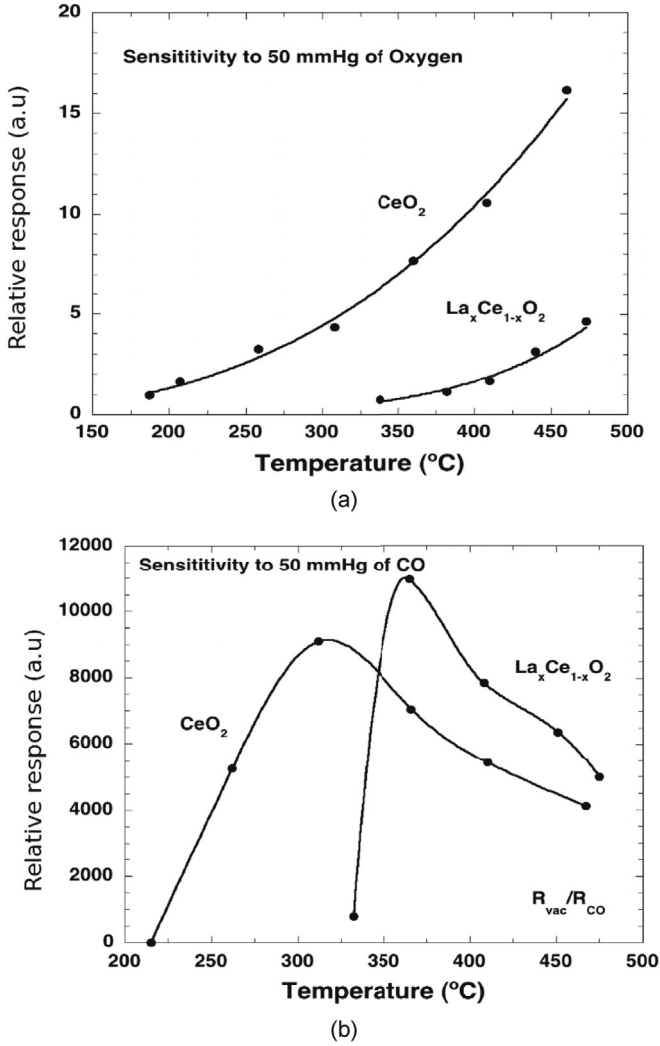**Fig. 5.** Relative response x Temperature (°C) for oxygen (a) and carbon monoxide (b) atmospheres.

conductivity as oxygen ionizes. Also, for temperatures greater than 300 °C, oxygen diffusion into the grain is facilitated and then oxygen vacancies in the bulk are annihilated. Interestingly, samples having La are less sensitive to oxygen. When the atmosphere is changed from vacuum to CO, a remarkable decrease of the electrical resistance is observed, especially on the La-sample. In Fig. 4b, we present the relative responses for CO exposure for doped and undoped samples. This is a consequence of the CO adsorption and reaction with superficial oxygen, indicating that CO is very efficient in increasing the film conductivity. The highest relative response for the La-doped film occurs between 350 °C and 400 °C.

Fig. 6 evidences the temporal electrical response of the samples after changing the atmosphere from vacuum to 50 mmHg of CO and then oxygen at 400 °C and later returning to vacuum. Resistance versus time curves can be understood by considering that acceptor levels at the intergrains are responsible for the observed electrical response. The increase of the resistance, when samples are exposed to oxygen, indicates that equilibrium at the surface is quickly reached. The interaction of oxygen with grain surfaces produces the transfer of electrons from the bulk to the surface moving also the difference of energy between the Fermi level and the 4f state at the band gap (E_{4f}–E_F). From this process, the density of carriers decreases and, as a consequence, the sample resistance increases. In previous work we have proposed that at
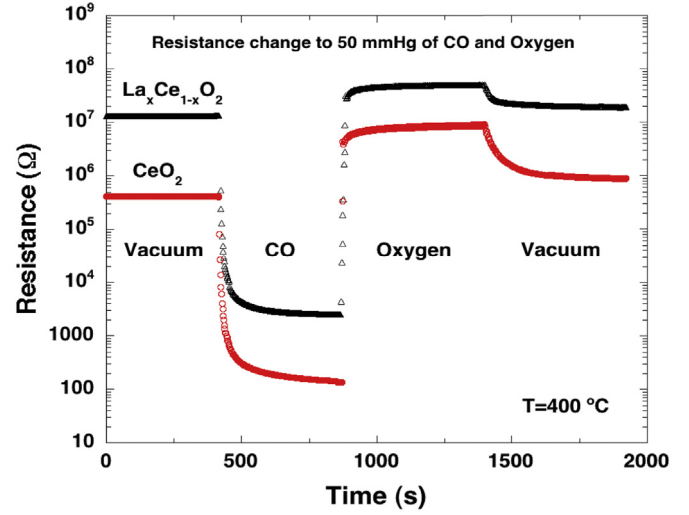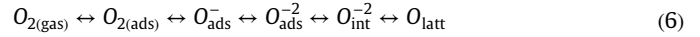

Fig. 6. Relative resistance x Time (s) for the film after exposure to Air or CO atmospheres, without vacuum, along with its response time.

temperatures high enough (greater than ~ 200 °C) the adsorbed oxygen onto the surface (charged oxygen species such O^-) can diffuse into the grains, annihilating oxygen vacancies and thus reducing the donor concentration [27]. Conversely, if oxygen diffuses out of the grains, vacancies are formed. The relevant reactions for oxygen from the gas phase to the bulk of the grain are [53]:
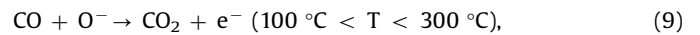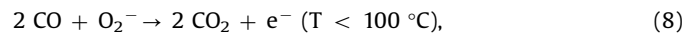
$$O_{2(gas)} \leftrightarrow O_{2(ads)} \leftrightarrow O_{ads}^- \leftrightarrow O_{ads}^{-2} \leftrightarrow O_{int}^{-2} \leftrightarrow O_{latt} \qquad (6)$$

where $O_{2(gas)}$ refers to oxygen in the environment, $O_{2adss)}$ to an oxygen molecule adsorbed at the grain surfaces, O_{ads}^- and O_{ads}^{-2} to singly and doubly ionized monatomic oxygen at the grain surface, O_{int}^{-2} to interstitial oxygen, and O_{latt}^{-2} to oxygen at the lattice. In the last part of Eq. (6), if surfaces are treated with a reducing reagent as CO, interstitial oxygen within the lattice migrates to the surface generating oxygen vacancies, V_o^{++}, i.e.:

$$O_{latt} \leftrightarrow V_o^{++} + O_{int}^{2-} \qquad (7)$$

Thus, after CO treatment at 400 °C, an increase in the oxygen vacancy concentration $[V_o^{++}]$ can be expected. At this point, it is necessary to remark that before performing the electrical measurements, the samples were previously inserted in air atmosphere due to their storage in ambient conditions, and probably had a high amount of oxygen adsorbed onto the surface and into the grains. Therefore, when samples are exposed to CO, the possible following processes can take place:

1) *CO adsorption.* Carbon monoxide adsorption on a clean surface produces an increasing of the barrier height and a diminution in the sample conductivity as shallow acceptors levels are generated.

2) *Reactions with CO.* At temperatures greater than 180 °C, carbon monoxide reacts with adsorbed oxygen on the CeO$_2$ surface according to following equations proposed by Ref. [54]:

$$2 \, CO + O_2^- \rightarrow 2 \, CO_2 + e^- \, (T < 100 \, °C), \qquad (8)$$

$$CO + O^- \rightarrow CO_2 + e^- \, (100 \, °C < T < 300 \, °C), \qquad (9)$$

$$CO + O_2^- \rightarrow CO_2 + 2 \, e^- \, (T > 300 \, °C), \qquad (10)$$

Worth to say that in order to minimize the content of oxygen species adsorbed at the surface, three cycles of heating up to 380 °C are made before each measurement itself. Therefore, the
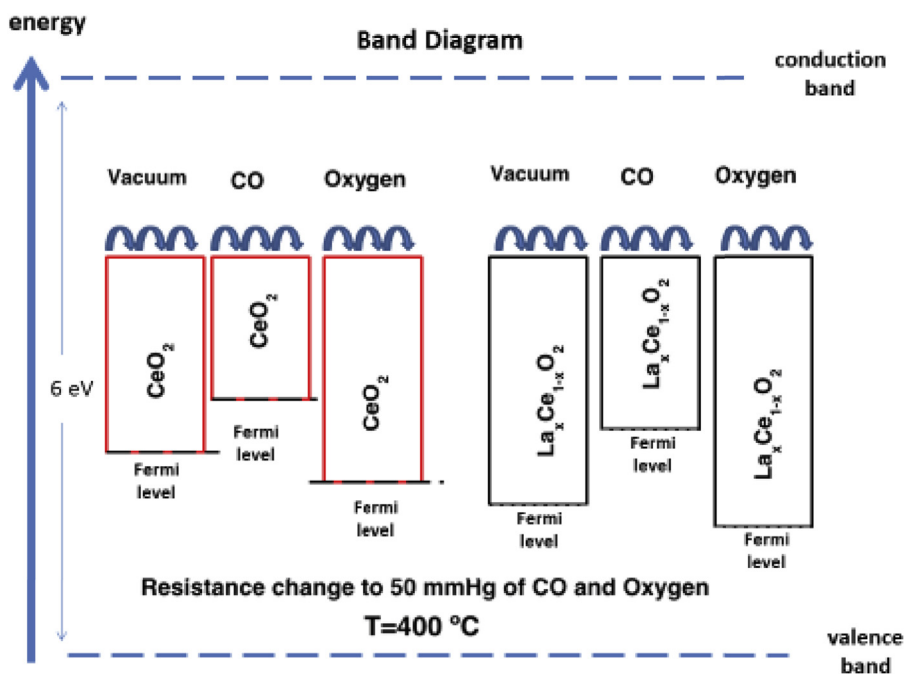
Fig. 7. Model for the hopping conduction mechanism of the pure and La-doped ceria nanostructures. For the sake of simplicity, the Fermi level is moved respect to the bands.
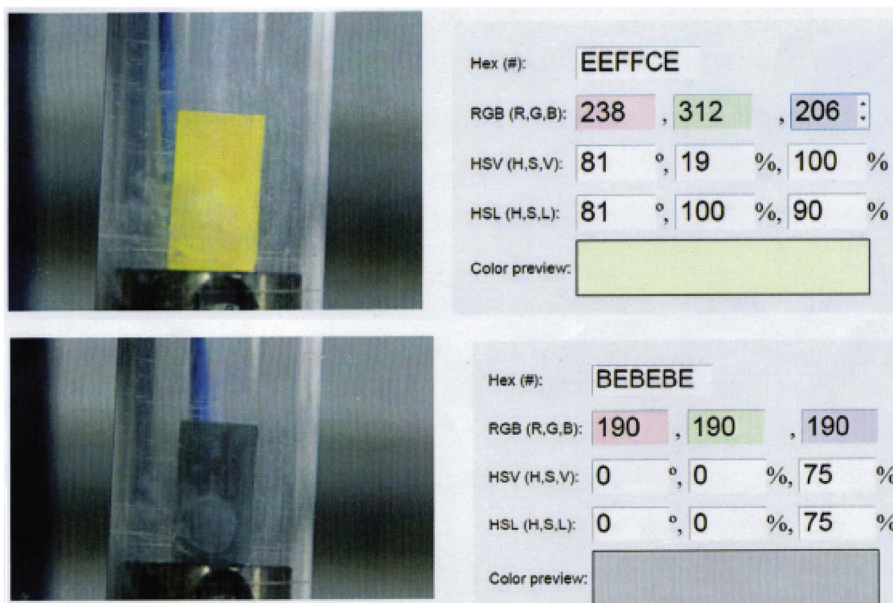

Fig. 8. Colour change of thick film as a function of CO exposure depicted by RGB photodiode. (For interpretation of the references to colour in this figure legend, the reader is referred to the web version of this article.)

electrical response is likely to be assigned to effects of CO exposure into the film surface, minimally related to oxygen desorption. After oxygen exposure, the oxygen diffusion into the grain takes place and the oxygen vacancy concentration is reduced. Then, due to a lower electron density, the sample conductivity decreases. At 400 °C, the oxygen diffusion into the grains is significant and the film responds immediately. Indeed, a relatively fast response time can be observed after both, oxygen and CO exposures, along with a resistance change. After that, a slight change can be observed, indicating that vacancies are created or annihilated as a consequence of the oxygen diffusion out or into the grains, respectively.

A band diagram, which corresponds to the electric conduction mechanism observed for pure and doped La samples is shown in Fig. 7. If we consider that the hopping mechanism is responsible for electrical conduction, then as a consequence of the oxygen absorption onto the surface along with oxygen diffusion into the grain (when samples are exposed to oxygen atmosphere) as well as oxygen reaction with CO (when samples are exposed to CO atmosphere), the energy difference between the Fermi level (E_F) and the 4f state (E_{4f}-E_F) moves in order to change the number of electrons available for conduction. At this point, we also need to consider the possible Ce^{+4} reduction to Ce^{+3} when samples are exposed to CO and the oxidation when samples are exposed to oxygen. Also, it can be noted that after La addition into the CeO_2 lattice, the sample conductivity (see resistance at t = 0 s, in Fig. 6) decreases. This could be explained as a reducing of electrons situated at 4f state responsible for electrical conduction.

Fig. 8 illustrates the semiconductor thick film exposure to CO atmosphere whereas is noted a change of colour in the visible spectrum as a function of temperature, around 380 °C. We believe that the behaviour of this physical property is related to the influence of microwave radiation on the [CeO$_8$] octahedron groups generated under a rapid heating and leads to a vibration on the charged particles. These factors probably result in a distortion process on the [CeO$_8$] and [LaO$_8$] octahedron groups, favouring the formation of intermediary energy levels within the band gap of this material. These energy levels are composed of oxygen 2p states (near the valence band) and lanthanum 3d states (below the conduction band). During the exposure to CO gas, some electrons are promoted from the oxygen 2p states to lanthanum 3d states through the absorption of heat. This mechanism results in the formation of self-trapped excitons (STEs), i.e., trapping of electrons (e−) by holes (h·). The emission process of photons (hν) occurs when an electron localized in a lanthanum 3d states decays into an empty oxygen 2p state. Consequently, the proposed mechanism for colour changes is based on the distortion process of [CeO$_8$] and [LaO$_8$] octahedron groups after CO exposure into the thick films. Also, this behaviour can be associated with the formation of superficial defects caused by the modifications on the morphology of these powders [55].

4. Conclusions

XRD results confirmed that the doped CeO$_2$ powder exhibited similar behaviour to the pure material already reported and could be well-indexed to a pure cubic structure of CeO$_2$ (space group: Fm3m) and point group symmetry O_h^5 with lattice constant a = 5.411 Å. The film presented a fast decrease of the resistance (for CO exposure) which is an indication of a rapid surface reaction. After that, a slow oxygen migration, from the lattice to the surface, creates oxygen vacancies that finally produce an increase in the sample conductivity as a consequence of a higher occupation of the 4f levels. The La-doped CeO$_2$ film sensor response originates from intrinsic defects and charge transfer after a certain degree of structural disorder. The dual sensor response is arising from the contribution of different intermediary energy levels within the band gap, likely associated with some electrons that are promoted from the oxygen 2p states to lanthanum 3d states through the absorption of energy (hν) along with a facile reduction of the Ce^{+4} atoms to Ce^{+3} due to an itinerant 4f electron. This mechanism results in the formation of self-trapped excitons (STEs), i.e., trapping of electrons (e−) by holes (h·). The emission process of photons (hν) occurs when an electron localized in a more energetic state, like lanthanum 3d, decays into a less energetic state, such as an empty oxygen 2p state. Consequently, the proposed mechanism for colour changes is based on the distortion process of [CeO$_8$] and [LaO$_8$] octahedron groups after CO exposure into the thick films.

Acknowledgments

References

[1] G. Wang, Q. Mu, T. Chen, Y. Wang, Synthesis, characterization and photo-luminescence of CeO$_2$ nanoparticles by a facile method at room temperature, J. Alloy. Comp. 493 (2010) 202–207.

[2] P. Bera, A. Gayen, M.S. Hegde, N.P. Lalla, L. Spadaro, F. Frusteri, F. Arena, Promoting effect of CeO$_2$ in combustion synthesized Pt/CeO$_2$ catalyst for CO oxidation, J. Phys. Chem. B 107 (2003) 6122–6130.

[3] G. Jacobs, L. Williams, U. Graham, D. Sparks, B.H. Davis, Low-temperature water-gas shift: in-situ DRIFTS - reaction study of a Pt/CeO$_2$ catalyst for fuel cell reformer applications, J. Phys. Chem. B 107 (2003) 10398–10404.

[4] R.X. Li, S. Yabe, M. Yamashita, S. Momose, S. Yoshida, S. Yin, T. Sato, Synthesis and UV-shielding properties of ZnO- and CaO-doped CeO$_2$ via soft solution chemical process, Solid State Ionics 151 (2002) 235–241.

[5] K. Sohlberg, S.T. Pantelides, S.J. Pennycook, Interactions of hydrogen with CeO$_2$, J. Am. Chem. Soc. 123 (2001) 6609–6611.

[6] P. Jasinski, T. Suzuki, H.U. Anderson, Nanocrystalline undoped ceria oxygen sensor, Sensor. Actuator. B Chem. 95 (2003) 73–77.

[7] F. Goubin, X. Rocquefelte, M.H. Whangbo, Y. Montardi, R. Brec, S. Jobic, Experimental and theoretical characterization of the optical properties of CeO$_2$, SrCeO$_3$, and Sr$_2$CeO$_4$ containing Ce^{4+} (f(0)) ions, Chem. Mater. 16 (2004) 662–669.

[8] D.G. Shchukin, R.A. Caruso, Template synthesis and photocatalytic properties of porous metal oxide spheres formed by nanoparticle infiltration, Chem. Mater. 16 (2004) 2287–2292.

[9] B. Djuricic, S. Pickering, Nanostructured cerium oxide: preparation and properties of weakly-agglomerated powders, J. Eur. Ceram. Soc. 19 (1999) 1925–1934.

[10] S. Dikmen, P. Shuk, M. Greenblatt, H. Gocmez, Hydrothermal synthesis and properties of Ce$_{1-x}$Gd$_{xO2}$-delta solid solutions, Solid State Sci. 4 (2002) 585–590.

[11] S.W. Zha, C.R. Xia, G.Y. Meng, Effect of Gd (Sm) doping on properties of ceria electrolyte for solid oxide fuel cells, J. Power Sources 115 (2003) 44–48.

[12] Y.R. Wang, T. Mori, J.G. Li, T. Ikegami, Low-temperature synthesis of praseo-dymium-doped ceria nanopowders, J. Am. Ceram. Soc. 85 (2002) 3105–3107.

[13] J.G. Li, T. Ikegami, Y.R. Wang, T.Mori, 10-mol%-Gd$_2$O$_3$-doped CeO$_2$ solid solutions via carbonate coprecipitation: a comparative study, J. Am. Ceram. Soc. 86 (2003) 915–921.

[14] M.J. Godinho, R.F. Goncalves, L.P.S. Santos, J.A. Varela, E. Longo, E.R. Leite, Room temperature co-precipitation of nanocrystalline CeO$_2$ and Ce$_{0.8}$Gd$_{0.2}$O$_{1.9}$-delta powder, Mater. Lett. 61 (2007) 1904–1907.

[15] R.A. Rocha, E.N.S. Muccillo, Preparation and characterization of Ce$_{0.8}$Gd$_{0.2}$O$_{1.9}$ solid electrolyte by polymeric precursor techniques, Adv. Powder Technol. Iii 416 (2003) 711–717.

[16] S. Wang, K. Maeda, Direct formation of crystalline gadolinium-doped ceria powder via polymerized precursor solution, J. Am. Ceram. Soc. 85 (2002) 1750–1752.

[17] F. Bondioli, A.B. Corradi, T. Manfredini, G. Leonelli, R. Bertoncello, Non-conventional synthesis of praseodymium-doped ceria by flux method, Chem. Mater. 12 (2000) 324–330.

[18] H.Z. Song, H.B. Wang, S.W. Zha, D.K. Peng, G.Y. Meng, Aerosol-assisted MOCVD growth of Gd$_2$O$_3$-doped CeO$_2$ thin SOFC electrolyte film on anode substrate, Solid State Ionics 156 (2003) 249–254.

[19] H. Wang, J.J. Zhu, J.M. Zhu, Liao, X.H. Xu, T. Ding, H.Y. Chen, Preparation of nanocrystalline ceria particles by sonochemical and microwave assisted heating methods, Phys. Chem. Chem. Phys. 4 4 (2002) 3794–3799.

[20] H.M. Yang, C.H. Huang, A.D. Tang, X.C. Zhang, W.G. Yang, Microwave-assisted synthesis of ceria nanoparticles, Mater. Res. Bull. 40 (2005) 1690–1695.

[21] M.M. Natile, G. Boccaletti, A. Glisenti, Properties and reactivity of nanos-tructured CeO$_2$ powders: comparison among two synthesis procedures, Chem. Mater. 17 (2005) 6272–6286.

[22] J.S. Lee, S.C. Choi, Crystallization behavior of nano-ceria powders by hydro-thennal synthesis using a mixture of H$_2$O$_2$ and NH$_4$OH, Mater. Lett. 58 (2004) 390–393.

[23] S. Komarneni, R. Roy, Q.H. Li, Microwave-hydrothermal synthesis of ceramic powders, Mater. Res. Bull. 27 (1992) 1393–1405.

[24] S. Komarneni, Q. Li, K.M. Stefansson, R. Roy, Microwave-hydrothermal processing for synthesis of electroceramic powders, J. Mater. Res. 8 (1993) 3176–3183.

[25] S. Komarneni, Q.H. Li, R. Roy, Microwave-hydrothermal processing for synthesis of layered and network phosphates, J. Mater. Chem. 4 (1994) 1903–1906.

[26] S. Komarneni, R. Pidugu, Q.H. Li, R. Roy, Microwave-hydrothermal processing of metal powders, J. Mater. Res. 10 (1995) 1687–1692.

[27] R.C. Deus, R.A.C. Amoresi, P.M. Desimone, F. Schipani, L.S.R. Rocha, M.A. Ponce, A.Z. Simoes, E. Longo, Electrical behavior of cerium dioxide films exposed to different gases atmospheres, Ceram. Int. 42 (2016) 15023–15029.

[28] A.B. Corradi, F.B. Bondioli, A.M. Ferrari, T. Manfredini, Synthesis and char-acterization of nanosized ceria powders by microwave-hydrothermal method, Mater. Res. Bull. 41 (1) (2006) 38–44.

[29] V. Abdelsayed, A. Aljarash, M.S. El-Shall, Z.A. Al Othman, A.H. Alghamdi, Mi-crowave synthesis of bimetallic nanoalloys and CO oxidation on ceria-sup-ported nanoalloys, Chem. Mater. 21 (2009) 2825–2834.

[30] H.L. Tuller, A.S. Nowick, Small polaron electron transport in reduced CeO2 single crystals, J Phys Chem Solids 38 (1977) 859–867, http://dx.doi.org/10.1016/0022-3697(77)90124-X.

[31] E. Wuilloud, B. Delley, W.D. Schneider, Y. Baer, Spectroscopic evidence for localized and extended f-symmetry states in CeO2, Phys. Rev. Lett. 53 (1984) 203–205.

[32] D.J. Kim, Lattice-parameters, ionic conductivities, and solubility limits in

fluorite-structure Hf-4+O2, Zr-4+O2, Ce-4+O2, Th-4+O2, V-4+O2 Oxide Solid-Solutions, J. Am. Ceram. Soc. 72 (1989) 1415–1421.

[33] S.J. Hong, A.V. Virkar, Lattice-parameters and densities of rare-earth-oxide doped ceria electrolytes, J. Am. Ceram. Soc. 72 (1995) 433–439.

[34] J.G. Li, T. Ikegami, T. Mori, T. Wada, Reactive $Ce_{0.8}RE_{0.2}O_{1.9}$ (RE = La, Nd, Sm, Gd, Dy, Y, Ho, Er, and Yb) powders via carbonate coprecipitation Synthesis and characterization, Chem. Mater. 13 (2001) 2921–2927.

[35] D.P. Fagg, J.C.C. Abrantes, D. Perez-Coll, P. Nuñez, V.V. Kharton, J.R. Frade, The effect of cobalt oxide sintering aid on electronic transport in $Ce_{0.80}Gd_{0.20}O_{2-\delta}$ electrolyte, Electrochim. Acta 48 (2003) 1023–1029.

[36] W. Huang, P. Shuk, M. Greenblatt, Hydrothermal synthesis and properties of $Ce_{1-x}Sm_xO_{2-x/2}$ and $Ce_{1-x}Ca_xO_{2-x}$ solid solutions, Chem. Mater. 9 (1997) 2240–2245.

[37] G. Wang, Q. Mu, T. Chen, Y. Wang, Synthesis, characterization and photo-luminescence of CeO_2 nanoparticles by a facile method at room temperature, J. Alloy. Comp. 493 (2010) 202–207.

[38] W.H. Weber, K.C. Hass, J.R. McBride, Raman study of CeO_2: second-order scattering, lattice dynamics and particle size effects, Phys. Rev. B 48 (1993) 178–185.

[39] M. Zawadzki, Preparation and characterization of ceria nanoparticles by mi-crowave-assisted solvothermal process, J. Alloy. Comp. 454 (2008) 347–351.

[40] P. Kubelka, F. Munk, Ein Beitrag zur optic der farbanstriche, Zeit. Fur. Tech. Physik 12 (1931) 593–601.

[41] S. Zhang, H.X. Fu, L.Y. Shi, C.S. Pan, Q. Li, Y.L. Chu, W.Y. You, Synthesis of CeO_2 nanorods via ultrasonication assisted by polyethylene glycol, Inorg. Chem. 46 (2007) 2446–2451.

[42] M. Hirano, M. Inagaki, Preparation of monodispersed cerium(IV) oxide parti-cles by thermal hydrolysis: influence of the presence of urea and Gd doping on their morphology and growth, J. Mater. Chem. 10 (2) (2000) 473–477.

[43] D. Wood, J. Tauc, Weak absorption tails in amorphous semiconductors, Phys. Rev. B 5 (1972) 3144–3151.

[44] N. Tibaldi, M.A. Ponce, P. Kalafatovich, H. Asencio, M.P. Desimone, A.Z. Simões, L.S.R. Rocha, E. Longo, A Device for the Optoelectronic Characterization of Materials, 2015, Argentina, 2015 0103953.

[45] N. Tibaldi, M.A. Ponce, P. Kalafatovich, H. Asencio, M.P. Desimone, A.Z. Simões, L.S.R. Rocha, E. Longo, A Device for the Optoelectronic Characterization of Materials, 2016, Brazil, 10 2016 028383 3.

[46] A.E. Morales, E.S. Mora, U. Pal, Use of diffuse reflectance spectroscopy for optical characterization of un-supported nanostructures, Rev. Mexic. de Física S 53 (2007) 18–22.

[47] V.M. Longo, L.S. Cavalcante, E.C. Paris, J.C. Sczancoski, P.S. Pizani, M.S. Li, J. Andres, E. Longo, J.A. Varela, Hierarchical assembly of $CaMoO_4$ nano-octa-hedrons and their photoluminescence properties, J. Phys. Chem. C 115 (2011) 5207–5219.

[48] S. Phokha, S. Pinitsoontorn, P. Chirauatkul, V. Poo-arporn, S. Maensiri, Synth-esis, characterization, and magnetic properties of monodisperse CeO_2 nano-sphere prepared by PVP-assisted hydrothermal method, Nano. Res. Let. 7 (2012) 425–437.

[49] L.S. Cavalcante, E. Moraes, M.A.P. Almeida, C.J. Dalmaschio, N.C. Batista, J. A. Varela, E. Longo, M. Siu Li, J. Andrés, B. Beltrán, A combined theoretical and experimental study of electronic structure and optical properties of β-$ZnMoO_4$ microcrystals, Polyhedron 54 (2013) 13–25.

[50] S. Phoka, P. Loakul, E. Swatsitang, V. Promarak, S. Seraphin, S. Maensiri, Synthesis, structural and optical properties of CeO_2 nanoparticles synthesized by a simple polyvinyl pyrolidone (PVP) solution route, Mater. Chem. Phys. 115 (2009) 423–428.

[51] M. Palard, J. Balencie, A. Maguer, J.-F. Hochepied, Effect of hydrothermal ri-pening on the photoluminescence properties of pure and doped cerium oxide nanoparticles, Mater. Chem. Phys. 120 (2010) 79–88.

[52] K. Singh, et al., Synergistic effects of ultrasonication and ethanol washing in controlling the stoichiometry, phase-purity and morphology of rare-earth doped ceria nanoparticles, Ultrason. Sonochem. 36 (2017) 182–190.

[53] M. Batzill, Surface science studies of gas sensing materials: SnO2, sensors (Basel), , 6 (10) (2006 Oct) 1345–1366.

[54] U. Weimar, W. Gopel, A.C. measurements on tin oxide sensors to improve € selectivities and sensitivities, Sens. Actuators B Chem. 26 (1995) 13–18.

[55] C.S. Ricardi, R.C. Lima, M.L. Dos Santos, P.R. Bueno, J.A. Varela, E. Longo, Solid State Ionic 118 (2009) 288–291.